The 9th European Congress on Computational Methods in Applied Sciences and Engineering
ECCOMAS Congress 2024
3–7 June 2024, Lisboa, Portugal

CRYOTWIN: TOWARDS THE INTEGRATION OF A PREDICTIVE FRAMEWORK FOR THERMAL DRILLING ECCOMAS CONGRESS 2024

DIPANKUL BHATTACHARYA[1], LEONARDO BOLEDI[1] AND JULIA KOWALSKI[1]

[1] Chair of Methods for Model-based Development in Computational Engineering (MBD)
RWTH Aachen University, 52056 Aachen, Germany
e-mail: {bhattacharya;boledi;kowalski}@mbd.rwth-aachen.de

Key words: Virtual Testbed, Thermal Melting Probes, Digital Twins, Multiphysics Modeling, Data Integration

Summary. The integration of data and simulations has become increasingly important in the design of physical systems. By developing a virtual replica that targets specific functions, a digital twin helps us control the key responses of the system and allows better insight into its functionality. Our application of interest consists of thermal drills or cryobots that access remote ice sheets and retrieve geophysical data, e.g., in Antarctica. Future exploration missions, however, will target the icy moons of our solar system, which requires extrapolating the performance of the cryobots to extreme environments and underlines the need for a virtual testbed, i.e., the Cryotwin. Physics-based forward models are a fundamental component of the Cryotwin. In particular, a hierarchy of computational models plays a key role in assessing the cryobot's efficiency, trajectory, and optimized sensor positioning. The numerical simulations are then integrated with a data hub to access environmental and measurement data. However, computing times present a difficult challenge when performing sensitivity analysis or real-time predictions during operations. Alternatively, we can employ surrogate models, e.g., Gaussian process emulation, to replace high-fidelity simulations. In this contribution, we present the Cryotwin structure and discuss its potential applications as a digital twin for cryobots, specifically focusing on efficiency prediction. Additionally, we analyze the effect of temperature-dependent ice properties on energy losses. By training a Gaussian emulator, we demonstrate a considerable reduction in compute time which opens opportunities for Cryotwin in the model-based design of future cryobots, mission preparation, and real-time operations.

1 INTRODUCTION

Thermal ice drilling gained popularity in the 1960s due to being less bulky and cleaner compared to mechanical drilling. As of today, it is still the favorite way of digging into the ice whenever the footprint needs to be minimized or autonomous operation is sought [2, 10]. The water beyond these ice layers has been preserved for a long time and constitutes a memory of past environmental conditions. Analyzing this water can help us better understand the biological aspects of the ecosystem that existed in that period. The observations from the Galileo probe in 1997 [2], which indicate the presence of water under the ice layer of Jupiter's moon Europa, give us the vision for a mission to extract the water beyond the ice layer in Europa to assess

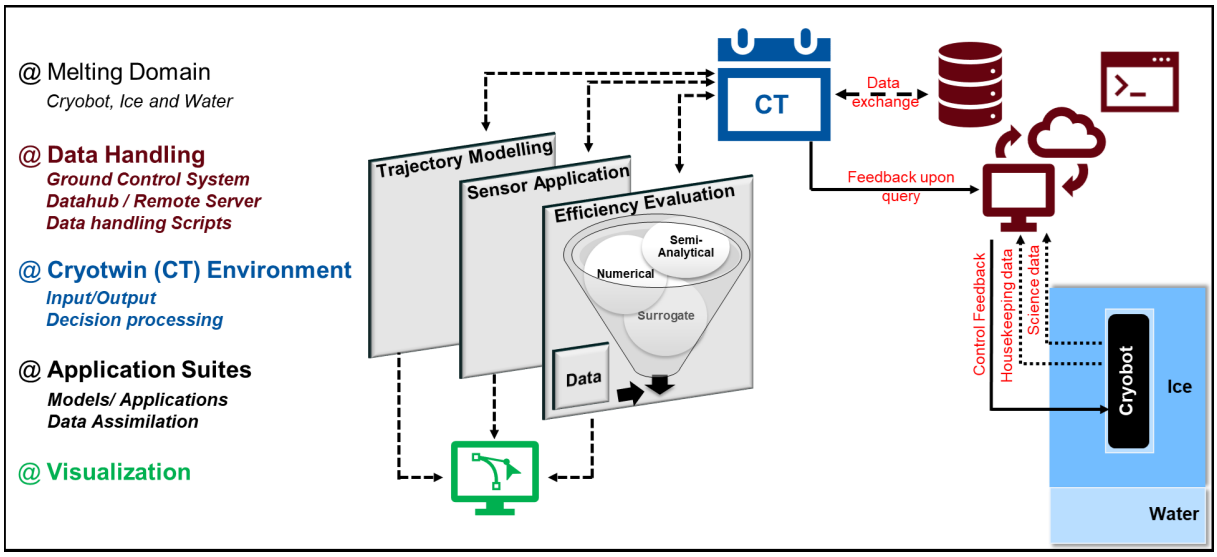

Figure 1: Sketch of the proposed Cryotwin structure. On the right, the physical melting process is shown. Data is collected and sent to the control system (brown). The Cryotwin (blue) processes the data and leverages computational models (black) for decision-making.

its potential habitability. To come up with a concept and plan for such a mission is extremely complex due to the unknown environmental conditions. Several lab-scale experiments performed in the 2000s examined low atmospheric pressure, heterogeneous ice, cryogenic ice, etc., but it is not established how well they will translate to an actual field test on Europa [10]. Given the uncertainties involved, it is of utmost importance to have a proper sensitivity analysis of the involved parameters in any model-based development of exploration technology that involves, e.g., efficiency modeling. Doing this in terms of lab experiments alone is not feasible. Also, autonomy becomes a necessary element of cryobots being developed for such extraterrestrial applications and demands real-time calculation for operation management. The digital twin concept leverages both physics and data-driven approaches and gives us control over the targeted behavior of the system based on two-way communication. This offers opportunities for model-based design and decision-making [11]. This motivates us to come up with a predictive digital twin – the Cryotwin – that would give us the possibility to conduct these experiments virtually.

The Cryotwin constitutes a virtualization of the cryobot that provides relevant simulation models and data along with digital infrastructure to efficiently interface its components. The theoretical Cryotwin concept, Fig. 1, can be realized on a single computer, or distributed hardware, that communicates with the cryobot. A local instance of an external datahub, similar to [7], is set up on the hosting computer and stores measurement data either from previous expeditions or from the cryobot, particularly for real-time assessments. The Cryotwin is interfaced with the datahub to use data for simulations and convey decisions via the hosting computer. Inside the Cryotwin three application areas are currently being worked on. Given a particular environmental condition, predict the trajectory and efficiency of the cryobot [12] and also use the Cryotwin to optimize sensor placement. Each of these application suites includes high and low-fidelity models identified as semi-analytical [3], numerical [9], and surrogate. Data assimilation strategies, such as using Kalman gain [13], are being worked on to improve calculated

states and predictions. For instance, surface temperature measurements in the cryobot can be used to correct the computed temperature and in turn, correct the calculated efficiency.

A description of the complete Cryotwin is beyond the scope of this contribution. Here, we will restrict ourselves to a description of Cryotwin's efficiency modeling suite. We present a semi-analytical model, extending the work in [3, 8], to predict the efficiency of the cryobot for applied heat and environment conditions, at a particular calculated probe velocity or melting velocity. While the model used here for efficiency prediction falls in the class of lower-fidelity models, it still offers similar in-type interfaces to alternative higher-fidelity models that will be coupled to the Cryotwin infrastructure as a next step [9]. Following that, we investigate the impact of state-dependent properties of ice on heat loss, which requires the numerical solution of nonlinear equations. This increases computing time and is unsuitable for real-time predictions or sensitivity analysis. Finally, we present a Gaussian emulator approach to reduce the computing time and discuss its future applications.

2 EFFICIENCY EVALUATION

2.1 Semi-analytical mathematical model

Mapping all the heat components that are involved with the domain is important for efficiency modeling. Fig. 2 shows the domain considered in this work. It includes the cylindrical axisymmetric melting head (the front part of the cryobot), the micro-scale melt film at the front, the melt channel at the side, and the ice around it. Fig. 3 shows the cross-section of the domain along with the heat components and geometrical parameters. Note that the applied heat Q_b, the melting heat Q_m, the lateral conductive heat loss to the ice Q_{lc}, and the convective heat loss via the melt channel Q_{cc} are on global thermal equilibrium, i.e., $Q_b = Q_m + Q_{lc} + Q_{cc}$. The other three components are internal to the system and implicitly satisfy equilibrium. Different process models based on the specific domain have been suggested in the past to predict the cryobot efficiency. The first efficiency model was developed by Aamot [1] and it involves the melting head and the surrounding ice and considers only Q_{lc}. Then, Schüller et al. analyzed the melt film and the effect of the gravitational force on the system [3]. The last approach, however, accounts for convective heat losses Q_c from the melt film only. In [8], the melt channel is considered explicitly, which allows to model both Q_{lc} and Q_{cc}. This time, however, the gravitational force is not considered, so different environmental conditions cannot be studied.

In this work, we consider the complete domain and both Q_{lc} and Q_{cc}, along with the effect of gravitational acceleration. We distinguish between two efficiency parameters. The first one is the close-contact melting (CCM) efficiency ϵ_{ccm}, as introduced in [3]. This term contains the effect of gravitational acceleration, but it is modified due to the presence of the melting channel. The second one is the total efficiency ϵ_{tot}. By definition, the total efficiency represents the fraction of the input power that is translated into forward motion, whereas the CCM efficiency captures how well the available heat in the melting head, hence after conductive losses Q_l, is translated into forward motion. Mathematically they are defined as

$$\epsilon_{ccm} = \frac{Q_m}{Q_f} \quad \text{and} \quad \epsilon_{tot} = \frac{Q_m}{Q_b}. \tag{1}$$

We subdivide our fluid domain into a horizontal channel representing the melt film and a vertical channel representing the melt channel. As the channels are thin, we simplify the

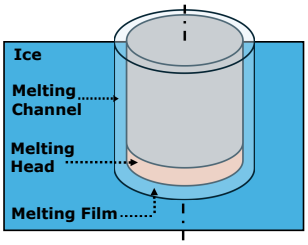

Figure 2: Sketch of the domain with the cryobot, melt film, and channel, along with the surrounding ice. The front part of the cryobot, the so-called melting head, supplies heat to the system.

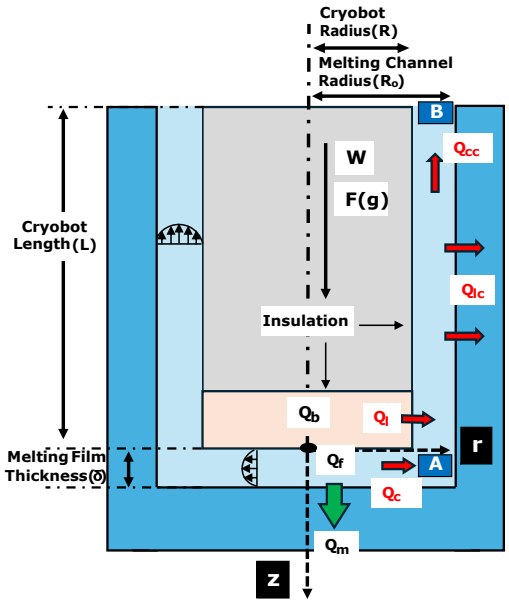

Q_b	Applied heat to the melting head
Q_f	Heat transferred from the melting head to the melt film
Q_m	Heat used for melting the ice
Q_c	Convective heat loss from melting film to melting channel
Q_l	Lateral Conductive heat loss from melting head to melting channel
Q_{lc}	Lateral conductive heat loss to the ice
Q_{cc}	Convective heat loss through the melting channel

Figure 3: Sketch of the cross-section of the melting domain with the heat components and parameters such as the radius of the cryobot and channel as well as the cryobot length and melting film thickness.

governing equations through lubrication theory [3]. We fix the cylindrical coordinate system at the center of the melting head surface, as shown in Fig. 3, such that the cryobot is stationary, whereas the ice is moving towards it with the melting velocity $-W$. Also, note that we consider a near-surface ice environment with constant ambient ice temperature. Following [1, 8], we consider only axial heating at the front and only radial heating at the lateral part of the domain. The mass, momentum, and energy conservation equations for the melt film are given by

$$\begin{aligned} \frac{1}{r}\frac{\partial(ru)}{\partial r} + \frac{\partial w}{\partial z} &= 0, \\ \mu\frac{\partial^2 u}{\partial z^2} &= \frac{\mathrm{d}p}{\mathrm{d}r}, \\ u\frac{\partial T}{\partial r} + w\frac{\partial T}{\partial z} &= \alpha_l\frac{\partial^2 T}{\partial z^2}, \end{aligned} \tag{2}$$

where μ is the dynamic viscosity and α_l is the thermal diffusivity of water. We consider boundary

conditions for the flow and temperature field at the surface of the melting head, i.e. $z = 0$,

$$u(r,0) = w(r,0) = 0, \quad \text{and} \quad \left.\frac{\partial T}{\partial z}\right|_{z=0} = -\frac{Q_f}{\pi R^2 k_l}, \tag{3}$$

and at the phase-change interface i.e. $z = \delta$,

$$u(r,\delta) = 0, \quad w(r,\delta) = -\frac{\rho_s}{\rho_l} W \quad \text{and} \quad T(r,\delta) = T_m, \tag{4}$$

where δ represents the melt film thickness, k_l is the thermal conductivity of water, ρ_s and ρ_l denote the densities of ice and water, and T_m is the melting temperature. To close the problem, the Stefan condition is considered for the energy balance at the phase-change interface, that is

$$\left.\frac{\partial T}{\partial z}\right|_{z=\delta} = -\frac{\rho_s}{k_l} W[h_m + c_{p,s}(T_m - T_s)], \tag{5}$$

where h_m is the latent heat of melting, $c_{p,s}$ is the heat capacity of ice and T_s is the ambient ice temperature. Using Eqs. (3) and (4) and integrating the mass and momentum terms in Eq. (2) across the melt film thickness, we get the pressure gradient and horizontal velocity

$$\frac{\mathrm{d}p}{\mathrm{d}r} = -\frac{6\mu \frac{\rho_s}{\rho_l} W r}{\delta^3} \quad \text{and} \quad u = -\frac{3\frac{\rho_s}{\rho_l} W r z(z-\delta)}{\delta^3}. \tag{6}$$

Similarly, integrating the energy equation by considering a parabolic temperature profile that satisfies the boundary conditions and Eq. (6), we obtain a relation for the melt film thickness

$$\delta = \frac{20\alpha_l \rho_l \left(\frac{Q_f}{R^2} - \frac{Q_m}{R_o^2}\right)}{W\rho_s \left(3\frac{Q_f}{R^2} + 7\frac{Q_m}{R_o^2}\right)}. \tag{7}$$

This relation allows us to infer the melt film thickness based on the melting velocity W and heat transferred from the melting head to the melt film Q_f. Note that differently from [3], this derivation includes the vertical melt channel of radius R_o. The melting heat Q_m is calculated from the Stefan condition

$$Q_m = \pi R_o^2 \rho_s W[h_m + c_{p,s}(T_m - T_s)]. \tag{8}$$

To derive another expression for δ, we first consider the force balance in the melt film

$$F(g) = \int_0^R \int_0^{2\pi} (p - p_o) r \, \mathrm{d}\phi \, \mathrm{d}r, \tag{9}$$

where p_o is the pressure at region B in Fig. 3. After integrating the pressure gradient in Eq. (6) and combining the pressure term with Eq. (9), we obtain another expression for melting film thickness

$$\delta = \left(\frac{1.5\mu\pi W R^4 \frac{\rho_s}{\rho_l}}{F(g) - \pi R^2 (p_1 - p_o)} \right)^{1/3}, \tag{10}$$

where p_1 denotes the pressure at region A in Fig. 3. Now, equating Eqs. (7) and (10), we obtain the CCM efficiency

$$\epsilon_{ccm} = \frac{Q_m}{Q_f} = \left(\frac{Ro^2}{R^2} \right) \frac{1 - \frac{3}{20\alpha_l} \left(\frac{WR\rho_s}{\rho_l} \right)^{4/3} \left(\frac{1.5\pi\mu}{F^*(g)} \right)^{1/3}}{1 + \frac{7}{20\alpha_l} \left(\frac{WR\rho_s}{\rho_l} \right)^{4/3} \left(\frac{1.5\pi\mu}{F^*(g)} \right)^{1/3}}. \tag{11}$$

Here, the net force F^* is given by $F^*(g) = F(g) - \pi R^2 (p_1 - p_o)$. To compute ϵ_{ccm}, we need to know W and p_1. The latter can be calculated by solving the flow field in the vertical channel, i.e., the melt channel. The momentum equation for the melt channel is given by

$$\frac{\mathrm{d}p}{\mathrm{d}z} = \frac{\mu}{r} \frac{\partial}{\partial r} \left(r \frac{\partial w}{\partial r} \right) + \rho_l g, \tag{12}$$

where g is the gravitational acceleration. We integrate Eq. (12) using the boundary conditions $w(R, z) = 0$ and $w(R_o, z) = -W$. Thus, we obtain the velocity in the melt channel

$$w = (R^2 - r^2)X + [-W + (R_o^2 - R^2)X] \frac{\ln\left(\frac{r}{R}\right)}{\ln\left(\frac{R_o}{R}\right)}. \tag{13}$$

The variable X is a function of p_1 and is given by

$$X = -\frac{1}{4\mu} \left(\frac{\partial p}{\partial z} - \rho_L g \right). \tag{14}$$

Equating the mass flow rate of melting ice and water flowing through the melt channel

$$\pi R_o^2 (-W) \rho_S = 2\pi \rho_L \int_R^{R_o} wr \, \mathrm{d}r, \tag{15}$$

we can finally calculate p_1 as a function of the unknown W. Now, to calculate W we use the global thermal equilibrium

$$Q_b = Q_m + Q_{lc} + Q_{cc}. \tag{16}$$

Q_m is given by Eq. (8). Q_{lc} and Q_{cc} are given as

$$
\begin{aligned}
Q_{lc} &= n\sigma^d[R_o^2 W(T_m - T_s)], \\
Q_{cc} &= \left(1 + 0.24021\frac{R_o - R}{R}\right)\frac{R_o - R}{2\alpha_l}\left(\frac{\pi R_o^2 \rho_s W}{\rho_l}\right)\left(\frac{ndL^{d-1}}{(WR_o^2)^d}R_o^2 W(T_m - T_s)\right),
\end{aligned} \tag{17}
$$

where $d = 0.726$ and $n = 932(\frac{2T_m}{T_m+T_s})$ are fit constants, and $\sigma = \frac{L}{WR_o^2} \in [5 \times 10^4, 10^8]$. We refer to [2, 4] for further details on the derivation of these equations.

To summarize the calculation process, for an applied heat Q_b and melting channel radius R_o, we solve the non-linear Eq. (16) to obtain the probe velocity W. Then, we can calculate Q_m, Q_{lc} and Q_{cc} to determine the total efficiency ϵ_{tot}. Using Eq. (15) and the velocity W, we obtain p_1 that is used to calculate ϵ_{ccm} with Eq. (11). Note that ϵ_{ccm} cannot be less than ϵ_{tot}. From Fig. 3 we see that the applied heat Q_b branches into heat going to the front part of the melting head Q_f and heat that is lost to the melt channel Q_l. Now as per Eq. (1), $\epsilon_{ccm} < \epsilon_{tot}$ would imply $Q_f > Q_b$, which would mean Q_l is negative, i.e., the melt channel is giving energy to the melting head. This is physically impossible within our application.

2.2 Variable material properties modeled by the non-linear heat equation

In the previous section, we used the formulation by Ulamec et al. [2], which considers ice properties at a representative ice temperature, i.e., $0.5(T_m + T_s)$. Considering near-surface ice with constant T_s, the temperature of ice close to the cryobot varies spatially, which influences, e.g., the thermal conductivity $k_s(T)$ [2]. To allow for spatially-varying material parameters, we have to go beyond the convenient semi-analytical model and leverage numerical tools like the finite element method (FEM) to calculate Q_{lc}. As we consider the steady state and also the melting head in a static frame of reference, the 2D heat equation in the ice at the lateral part of the cylindrical cryobot is given as

$$
\frac{1}{r}\frac{\partial}{\partial r}\left(-k_s(T) r \frac{\partial T}{\partial r}\right) + c_s(T)\rho_s(T) W \frac{\partial T}{\partial z} = 0. \tag{18}
$$

This non-linear 2D equation can be converted into a non-linear transient 1D equation, by introducing time $t = \frac{z}{W}$, which yields

$$
\frac{1}{r}\frac{\partial}{\partial r}\left(-k_s(T) r \frac{\partial T}{\partial r}\right) + c_s(T)\rho_s(T) \frac{\partial T}{\partial t} = 0. \tag{19}
$$

We solve Eq. (19) for the end time given by $\frac{L}{W}$ and obtain the heat flux q_{lc} along the length of the ice surface. Then, we integrate it over the cylindrical curve surface to get the total heat loss

$$
Q_{lc} = 2\pi R_o \int_0^L q_{lc}(l)\,\mathrm{d}l. \tag{20}
$$

2.3 Surrogate based on Gaussian emulation as real-time enabler

Experiments and numerical solution strategies are not suitable for real-time prediction or sensitivity analysis of efficiency values. Surrogates for numerical models can be used to reduce the computational time. Within this work, we focus on Gaussian process emulation, namely, a stochastic algorithm that uses multi-variate Gaussian functions to represent model output.

The mathematical description of the algorithm is beyond the scope of this work, the reader is referred to [5, 6] for further details on Gaussian processes. For our emulator, we use a first-order polynomial trend and the Matern-5-2 correlation function. For the hyperparameters, we use a cross-validation estimator and a hybrid genetic algorithm for the optimization process.

Evaluating the Cryotwin's efficiency model, at present, involves providing the geometrical parameters of the cryobot (see Fig. 3), mass, applied heat Q_b and selecting planetary conditions. The Gaussian emulator is trained with the FEM solutions for updated conditions at regular intervals and is recommended for fast evaluation of Q_{lc}. The Cryotwin outputs the probe or melting velocity, the heat components, and the efficiency values for specified input conditions.

3 RESULTS AND DISCUSSION

We use the Cryotwin to assess the performance of a cryobot of mass 30 kg, Length $L = 2.5$ m, Radius $R = 0.06$ m with melting channel thickness 0.003 m that makes $R_o = 0.063$ m, on Earth and Europa. We first obtain the heat components and efficiencies, as described in Section 2.1 and given in Eqs. (16) and (1). Then, we assess the effect of spatially varying temperature on heat loss using the Cryotwin FEM solver as described in Section 2.2. Further, we use the Cryotwin Gaussian emulator to build a surrogate for the numerical solver following Section 2.3.

3.1 Energy loss and efficiency

Fig. 4 shows the calculated heat components on Earth and Europa. The applied heat Q_b is on the x-axis, and the fraction of heat components to Q_b is on the y-axis. Additionally, we show the probe velocity W on the right y-axis, which is solved using the non-linear Eq. (16). From both plots, we see that the conductive heat loss Q_{lc} is substantially higher than the convective heat loss Q_{cc}. At lower Q_b, the maximum amount of heat is getting lost rather than being used for melting. As we increase Q_b, the fraction of melting heat Q_m increases causing an increase in W and a reduction in the Q_{lc} fraction. However, the Q_{cc} fraction increases, because as the velocity W increases, the flow through the melt channel increases. This is to remove the increasing amount of water produced by the faster melting process through the fixed-width channel. When we compare the plots between Earth and Europa, we observe that a much higher amount of Q_b is required to attain the same W. Also, the fraction of heat being lost (both Q_{lc} and Q_{cc}) is higher on Europa than on Earth. This can be attributed to the much colder ice found on Europa (100 K) compared to Earth (220 K).

Fig. 5 shows the total efficiency ϵ_{tot} and the CCM efficiency ϵ_{ccm} for both Earth and Europa. On the x-axis, we have Q_b, on the y-axis we have the efficiencies, and on the right y-axis, we have W. Both plots show that ϵ_{tot} increases as we increase Q_b. This is directly related to the increase of Q_m, as evident in Fig. 4. Also, we see a decrease in ϵ_{ccm} as we increase Q_b. This is because as Q_b increases so does W and the amount of water generated from melting ice. A higher pressure is required to remove the increasing amount of water through the fixed-size melting channel. This increases the total pressure in the melting film and reduces the net force $F^*(g)$ acting

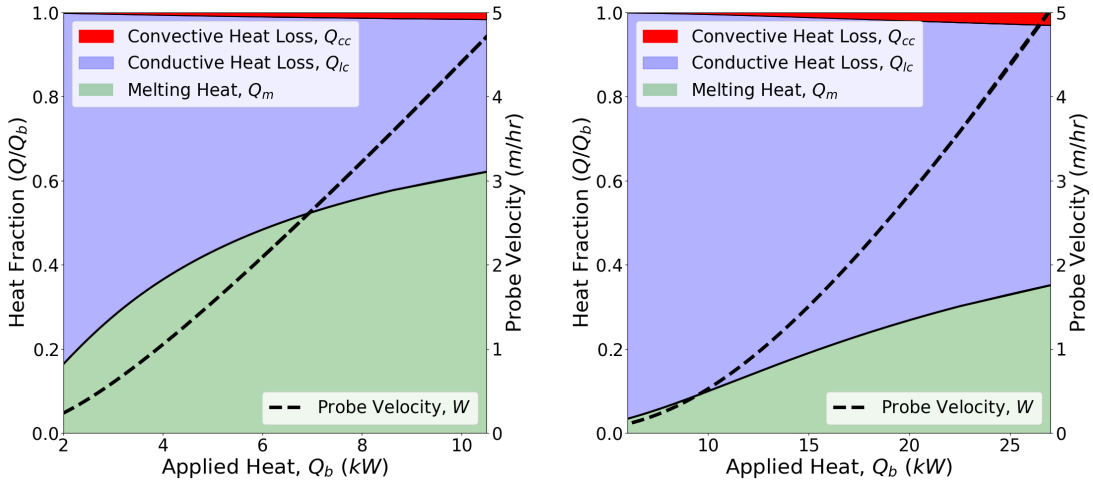

(a) Earth

(b) Europa

Figure 4: Fraction of heat components Q_{cc}, Q_{lc} and Q_m to applied heat Q_b for Earth (a) and Europa (b).

downwards. And finally, since the ϵ_{ccm} is directly proportional to $F^*(g)$, as shown in Eq. (11), we see it decreasing. Based on the fact that $\epsilon_{ccm} < 1$ and $\epsilon_{ccm} > \epsilon_{tot}$, as explained previously, we obtain a theoretical limit on the achievable W, as shown in Fig. 5. Thus, given a particular environmental condition, i.e., Earth or Europa, and a particular melting channel configuration, we can achieve a certain possible range of W for a corresponding Q_b range. When we compare the plots for Earth and Europa, we see a direct translation of Q_m plots from Fig. 4 into the ϵ_{tot} plots. The presence of much colder ice explains the observed lower ϵ_{tot} in the case of Europa. We also observe a range with lower W values in the case of Europa (0.6-4.2 m/hr) against Earth (1-4.4 m/hr). This is explained by the presence of lower gravitational acceleration on Europa (1.3 m/s^2) compared to Earth (9.8 m/s^2), which reduces the net force $F^*(g)$ to begin with. From thermal equilibrium, see Fig. 4, any value of W is possible when subjected to corresponding Q_b. However, when we overlap this with force balance and bring in the concept of ϵ_{ccm}, we get a physically possible range of W. Also, it is quite counter-intuitive how the velocity increases within this range without an expected asymptotic behavior towards the limits. This is because we consider a fixed melting channel radius. The Q_b beyond this range would presumably change the channel configuration, which can be captured via high-fidelity numerical simulations and is part of our future research.

3.2 Effect of temperature-dependent ice properties

As witnessed in Fig. 4, Q_{lc} forms a major part of Q_b. Fig. 6 shows Q_{lc} for different calculated W. We call the analytical solution by Aamot [1], which considers constant ice properties at melting temperature T_m, as sol. 1, and the analytical solution by Ulamec [2], given by Eq. (17), as sol. 2. Next, we have the FEM 1D linear solution, by solving Eq. (19) but with constant ice properties at T_m. We call this sol. 3. And lastly, the FEM 1D non-linear solution, obtained

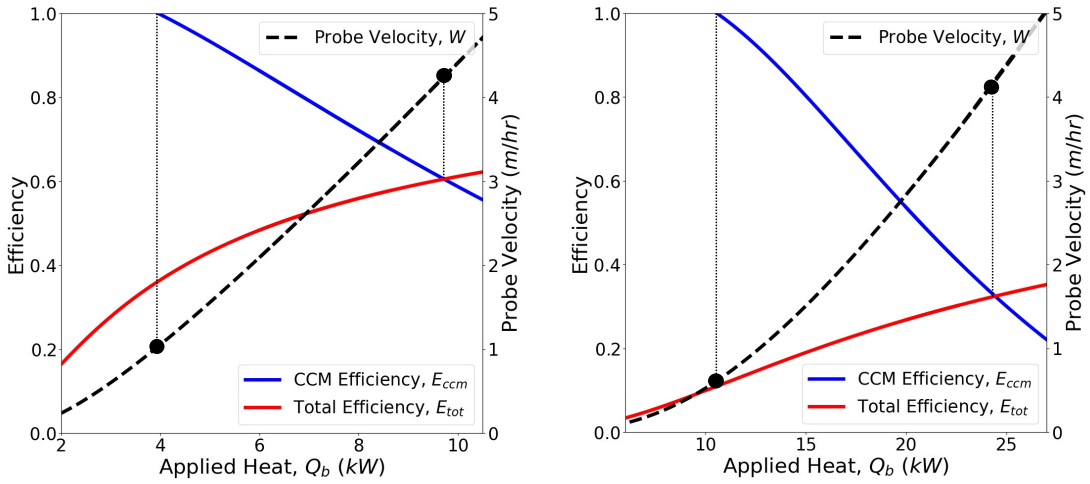

(a) Earth (b) Europa

Figure 5: Total and CCM efficiency along with velocity W at applied heat Q_b for Earth (a) and Europa (b).

by solving Eq. (19), is referred to as sol. 4. From plots for both Earth and Europa, we can see that sols. 1 and 3 underestimate Q_{lc}, which underlines the effect of considering temperature-dependent ice properties. This is even more prominent in the case of Europa, where we have much colder ice. Also, sol. 2 shows a good resemblance with sol 4 at lower W values and comparatively warmer ice, like on Earth. However for colder ice, like on Europa, we can already see a deviation of sol. 2 from 4 even at lower W. At higher W values we notice an underestimation of Q_{lc} by sol. 2 for both Earth and Europa, being significant for the case of colder ice on Europa. Empirical data shows underestimation up to 50% by sol. 1 in the case of colder ice as mentioned in [8]. A similar observation is made when we compare sols. 1 and 4 for Europa in Fig. 6.

3.3 Gaussian prediction

As we showed in the previous section, considering temperature-dependent ice properties is paramount for calculating Q_{lc} and involves solving the non-linear heat equation. For instance, on a Lenovo Thinkpad $i7$ Laptop with 16 GB RAM and serial implementation, the time required to obtain the analytical solution for Q_{lc} is 0.5 s, the linear and non-linear 1D FEM solution is 0.7 s and 89 s, respectively. This adds a lot of overhead when planning for sensitivity analysis or real-time prediction of Q_{lc}. We set up the Gaussian process emulator by training it with 100 points of W and T_s as inputs and corresponding Q_{lc} as the output, being calculated using the 1D Non-Linear Eq. (19). We also add a noise of 0.1 kW in the output training data to check the robustness of the emulator. Fig. 7 shows the prediction of the emulator on 20 completely different points (other than training points) along with the 1D non-linear FEM solution at those same points. We observe a good mean prediction by the emulator along with a maximum standard deviation (uncertainty) of 0.42 kW and an average of 0.14 kW. These values can be further reduced by using the active learning strategy. Further, Table 1 shows the time associated

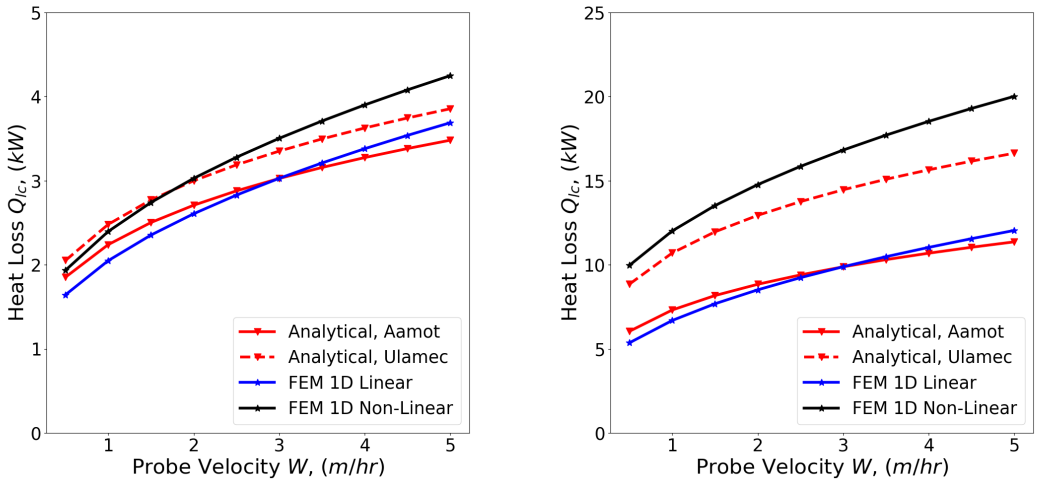

(a) Earth (b) Europa

Figure 6: Effect of temperature-dependent ice properties on lateral conductive heat loss Q_{lc} at a constant ambient temperature T_s for Earth (220 K) and Europa (100 K).

with each part of the Gaussian emulator. By using the emulator, we could reduce the computing time, i.e., calculate Q_{lc} and at the same time maintain good prediction accuracy.

Table 1: Time components (in seconds) involved during the setup of the Gaussian emulator.

Training Data generation	Training	Ground Truth Data generation	Prediction
89×100	2.2	89×20	0.65

4 CONCLUSIONS

In this work, we presented the Cryotwin concept and its efficiency modeling suite. We derived a semi-analytical efficiency model, extending existing results, that allows us to evaluate the effect of the melt channel on the cryobot's performance for different environmental conditions. The introduction of a fixed width melt channel not only brings in additional components of heat loss but, when combined with ϵ_{ccm}, establishes a theoretical limit on dynamics of the cryobot, i.e., its velocity W. The Cryotwin can also consider spatial variation of ice properties via its numerical solver, which plays a significant role in quantifying Q_{lc}, especially in colder ice environments like Europa. Runtime challenges with the numerical solver are tackled with the Cryotwin Gaussian emulator that provides an accurate and fast prediction of Q_{lc}. The initial analysis presented supports Cryotwin's suitability in model-based design of future cryobots, mission preparation, and real-time operations and therefore will be extended further to enhance its capabilities.

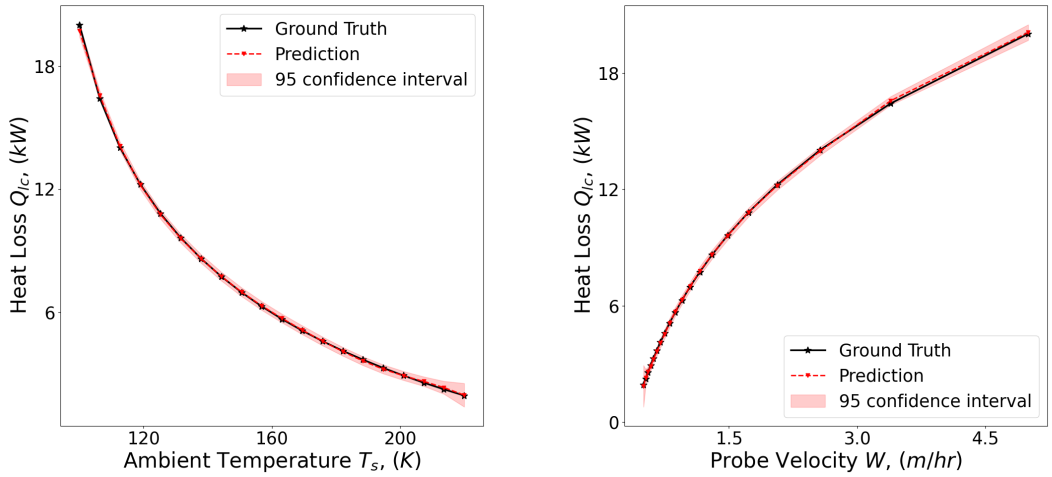

Figure 7: Prediction of lateral conductive heat loss Q_{lc} at different ambient temperature T_s (a) and probe velocity W (b).

5 ACKNOWLEDGEMENTS

This project is a part of the TRIPLE project line and is funded by the German Space Agency at DLR and the German Federal Ministry for Economic Affairs and Climate Action.

REFERENCES

[1] H.W.C. Aamot, Heat Transfer and Performance Analysis of a Thermal Probe for Glaciers, *Technical Report, Cold Regions Research and Engineering Laboratory, Hanover New Hampshire*, 194 (1967).

[2] S. Ulamec et al., Access to glacial and subglacial environments in the Solar System by melting probe technology. *Rev Environ Sci Biotechnol* 6 (2007) 71-94, doi: 10.1007/s11157-006-9108-x.

[3] K. Schuller et al., Melting probe technology for subsurface exploration of extraterrestrial ice Critical refreezing length and the role of gravity. *Icarus* 317 (2019) 1-9, doi: 10.1016/j.icarus.2018.05.022.

[4] B. Cassler et al., Constraints on the behavior of a descending ice probe due to force balance. *Acta Astronautica* 189 (2021) 606-614, doi: 10.1016/j.actaastro.2021.09.002.

[5] C. Lataniotis et al., Uncertainty Quantification in the cloud with UQCloud. *Inter. Conf. on Uncertainty Quantification in Comp. Sci. and Eng.* (2021).

[6] H. Zhao., Gaussian processes for sensitivity analysis, Bayesian inference, and uncertainty quantification in landslide research. *Dissertation / PhD Thesis, RWTH Aachen University* (2021), doi: 10.18154/RWTH-2021-11693.

[7] A. Simson et al., Enriched metadata for hybrid data compilations with applications to cryosphere research, *Helmholtz Metadata Collaboration Conference*, online, October 5-6, doi: 10.5281/ZENODO.7185422 (2022).

[8] M.J. Durka et al., Modeling a class of thermal ice probes for accessing the solar system's ocean worlds. *Acta Astronautica* 193 (2022) 483-495, doi: 10.1016/j.actaastro.2021.12.018.

[9] L. Boledi et al., A scale-coupled numerical method for transient close-contact melting. *Computers & Mathematics with Applications* 143 (2023), pp. 277–288.

[10] B. Dachwald et al., Chapter 29: Ice Melting Probes. *Handbook of Space Resources* (2023), doi: 10.1007/978-3-030-97913-3.29.

[11] National Academies of Sciences, Engineering, and Medicine. 2024. *Foundational Research Gaps and Future Directions for Digital Twins.* Washington, DC: The National Academies Press. doi: 10.17226/26894.

[12] F. Baader et al., Field-test performance of an ice-melting probe in a terrestrial analogue environment. *Icarus* 409 (2024) 115852, doi: 10.1016/j.icarus.2023.115852.

[13] L. Donato et al., Self-updating digital twin of a hydrogen-powered furnace using data assimilation. *Applied Thermal Engineering* 236 (2024) 121431, doi: 10.1016/j.applthermaleng.2023.121431.